Wide-angle X-ray scattering study of the lamellar/fibrillar transition for a semi-crystalline polymer deformed in tension in relation with the evolution of volume strain

Laurent Farge, Julien Boisse, Jérôme Dillet, Stéphane André, Pierre-Antoine Albouy, Florian Meneau

Wide-Angle X-ray Scattering Study of the Lamellar/Fibrillar Transition for a Semi-crystalline Polymer Deformed in Tension in Relation with the Evolution of Volume Strain

Laurent Farge,[1] Julien Boisse,[1] Jérôme Dillet,[1] Stéphane André,[1]
Pierre-Antoine Albouy,[2] Florian Meneau[3]

[1]Laboratoire d'Energétique et de Mécanique Théorique et Appliquée, CNRS UMR 7563 – Lorraine University, F-54500 Vandoeuvre lès Nancy, France
[2]Laboratoire de Physique des Solides, Université Paris-Sud and CNRS, UMR 5302, 91405 Orsay, France
[3]Soleil Synchrotron, Swing Beamline L'Orme des Merisiers, 91190 Saint-Aubin, France

ABSTRACT: This work is devoted to the study of the deformation mechanisms of a high density polyethylene deformed in tension. Specific treatments were applied to synchrotron wide angle X ray scattering patterns obtained *in situ* with the aim of quantifying: (i) the evolution of the apparent crystal sizes during the deformation process, (ii) the reorientation dynamics of the fragmented crystals while aligning their chains along the drawing axis during the establishment of the fibrillar morphology, and (iii) the reorientation dynamics of the amorphous chains. In addition, the volume strain evolution was measured using 3D digital image correlation. The cavitation phenomenon was found to mainly occur during the lamellae fragmentation phase. At the end of the deformation process, when the lamellar structure is destroyed, the fragmented crystals have new degrees of freedom and become free to rotate to align their chains along the drawing axis. Crystal fragmentation is then no longer needed to allow material deformation, and there is no further volume strain increase. © 2015 Wiley Periodicals, Inc. J. Polym. Sci., Part B: Polym. Phys. **2015**, *53*, 1470 1480

KEYWORDS: deformation mechanisms; high density polyethylene; necking; polyethylene (PE); semi crystalline polymers; strain; volume strain; WAXS

INTRODUCTION At the undeformed state, the crystalline parts of the semi-crystalline polymers (SCPs) have a lamellar morphology. They are made of stacks of parallel crystalline lamellae separated by amorphous regions. At the specimen scale, the orientation of the lamellae stacks is uniformly distributed. At a much smaller scale, the lamellae have been found not to be perfect crystals but instead have a granular substructure corresponding to an agglomeration of individual crystal blocks.[1–3] This blocky substructure is essential if we are to understand the plastic deformation mechanisms of the lamellae.

Numerous studies have aimed to determine the deformation mechanisms that occur at the lamellae level for SCPs deformed in tension (see Galeski[4] for a review). Before the yield point (true strain 0:1), the deformation first occurs in the amorphous phase. The main associated deformation mechanisms are: lamellar separation, lamellae stack rotation, and interlamellar slips. However, relatively minor plastic deformation can still occur in lamellae before the yield point. Strobl and coworkers found that this preyield point plastic deformation is due to isolated slips of crystalline blocks within the lamellae and only corresponds to a small part of the total strain.[5–10] Above the yield point, the crystalline blocks slips are no longer isolated and become collective instead, which means that the plastic deformation of the lamellae can be viewed as a major mechanism in the whole material deformation process. The lamellar structure is preserved overall up to a true strain value of roughly 0.5 after which the lamellae undergo coarse slips, leading to lamellae fragmentation.[5] Next, the morphology becomes progressively fibrillar: the lamellae are fragmented into small blocks coupled by tie molecules and reorient to align their chains along the drawing axis.

The way the fibrillar morphology is established is linked with specific transformations of the wide-angle X-ray scattering (WAXS) patterns obtained during the deformation process. First, the crystal fragments and their sizes decrease, which results in significant broadening of the diffraction peaks. Second, the alignment of chains along the drawing axis causes

the X-ray intensity arising from both the amorphous region and the crystallographic planes parallel to the chains to be concentrated along the direction that is perpendicular to the drawing axis. For high-density polyethylene (HDPE), the characteristic WAXS patterns corresponding to the fibrillar morphology have generally been observed for true strain values significantly larger than 1.3.[5,11–14]

In addition, for the SCPs deformed in tension, the cavitation phenomenon may occur during certain specific stages of the deformation process.[14,15] Logically, the cavitation phenomenon causes an increase in volume strain, which means that analysis of volume strain evolution during the deformation process can provide valuable insight about the microstructural transformations in progress. Some studies based on volume strain measurements and on scanning electron microscopy observations suggest a direct link between cavitation and lamellae fragmentation. For example, Addiego et al.[16] have shown qualitatively that inhomogeneous deformation mechanisms of spherulites caused by lamellae fragmentation are associated with a strong volume strain increase. For an oriented HDPE, Ruihua et al.[17] have shown that irreversible volume strain begins at the onset of lamellae fragmentation. Furthermore, as Galeski[4] and Pawlak et al.[15] noted, the Peterlin representation,[18] which is widely used to provide simple descriptions of the destruction of lamellar morphology, inherently implies cavitation.

In addition to the aforementioned deformation mechanisms, when polyethylene is subjected to tensile drawing, the martensitic transformation takes place during the deformation process. This corresponds to the transformation of a part of the polyethylene crystals from an orthorhombic crystallographic form to a monoclinic form.[11,12,19–21]

For a HDPE subjected to tensile loading, the major objective of this work was to show the links between phenomena occurring at the crystal level during the deformation process and certain macroscopic observables, in particular volume strain. Specific data processing methods were developed to extract quantitative data from WAXS patterns. These enable the description of some major aspects characterizing the lamellar/fibrillar transition, namely the reduction in crystal size due to fragmentation and the reorientation dynamics of the fragmented crystals and amorphous chains. With synchrotron radiation, it was possible to acquire the variables quantifying these phenomena as a function of the longitudinal strain in a "quasi-continuous" way. This makes it possible to accurately determine the thresholds separating the different regimes observable on the obtained curves. The volume strain measurements were obtained using 3D digital image correlation (DIC) a technique previously proved to give very accurate volume strain measurements.[22]

EXPERIMENTAL

Material

The SCP studied in this work is a HDPE produced by Röchling Engineering Plastics KG (grade "500 Natural"). The specimens were manufactured by extrusion. Information from the supplier gave the molecular weight and density as 500,000 g mol^{-1} and 0.95 g cm^{-3}, respectively. Differential scanning calorimetry yields a crystallinity index of about 68 wt % for this SCP. Synchrotron small-angle X-ray scattering experiments enabled a morphological characterization of the undeformed material: crystalline phase thickness 18.5 nm and amorphous layer thickness 8.2 nm. The yield stress was of the order of 33 MPa corresponding to a value of 0.1 for the yield strain.

A 6 mm length flat part was machined on the specimen lateral faces to promote a uniaxial stress state in the center of the specimen. The central cross-section of the specimen used for the volume strain measurements was $6 \times 6\,mm^2$ and $3 \times 3\,mm^2$ for the WAXS experiments. With this geometry, the necking phenomenon starts in the specimen central region, which was exactly where the WAXS measurement was obtained. The specimen deformation evolution is characterized by the value of the true longitudinal strain ε_{11} $\ln(l/l_0)$ measured in the specimen center. Axis 1 corresponds to the tensile axis.

Wide-Angle X-ray Scattering

The WAXS experiments were performed at "Soleil Synchrotron" (Swing beamline). The sample detector distance was 498 nm, and the wavelength was 0.077488 nm. The *in-situ* WAXS experiments were carried out using a Kammrath & Weiss tensile minimachine (5 kN), specifically conceived for synchrotron studies. The two cross-heads are mobile and move apart at the same speed, which means that the synchrotron beam always crosses the specimen in its central cross-section throughout the tensile test. The relative cross-heads speed was 20 $\mu m\ s^{-1}$ (average strain rate of the order of $2.5 \times 10^{-3}\ s^{-1}$). During the experiments, 100 WAXS measurements were obtained with constant delays between two consecutive measurements (10 s).

3D Digital Image Correlation

The 3D-DIC technique is a whole-field strain measurement method. It is based on the stereo-correlation principle, which means it can be used to perform measurements on a non-plane surface. For this study, we used the 3D-DIC Aramis® device provided by GOM-Instruments. A random speckle was applied to the specimen using an air brush. We used 40×40 pixels facets and an 8 pixels stepsize (distance between two adjacent facets). The strain reference length[22] was thus 16 pixels and one pixel represented approximately 16 μm on the specimen.

The 3D-DIC technique was used to measure the volume strain in the specimen central cross-section. This article provides a relatively simple summary of the experimental procedure because it has already been described in detail in two previous articles where we provide full analyses of the Poisson's ratio and of the volume strain measurements[23] as well as a study of the kinematics of the necking phenomenon.[24] During a tensile test, simultaneous strain measurements were made on two perpendicular faces of a specimen. The longitudinal

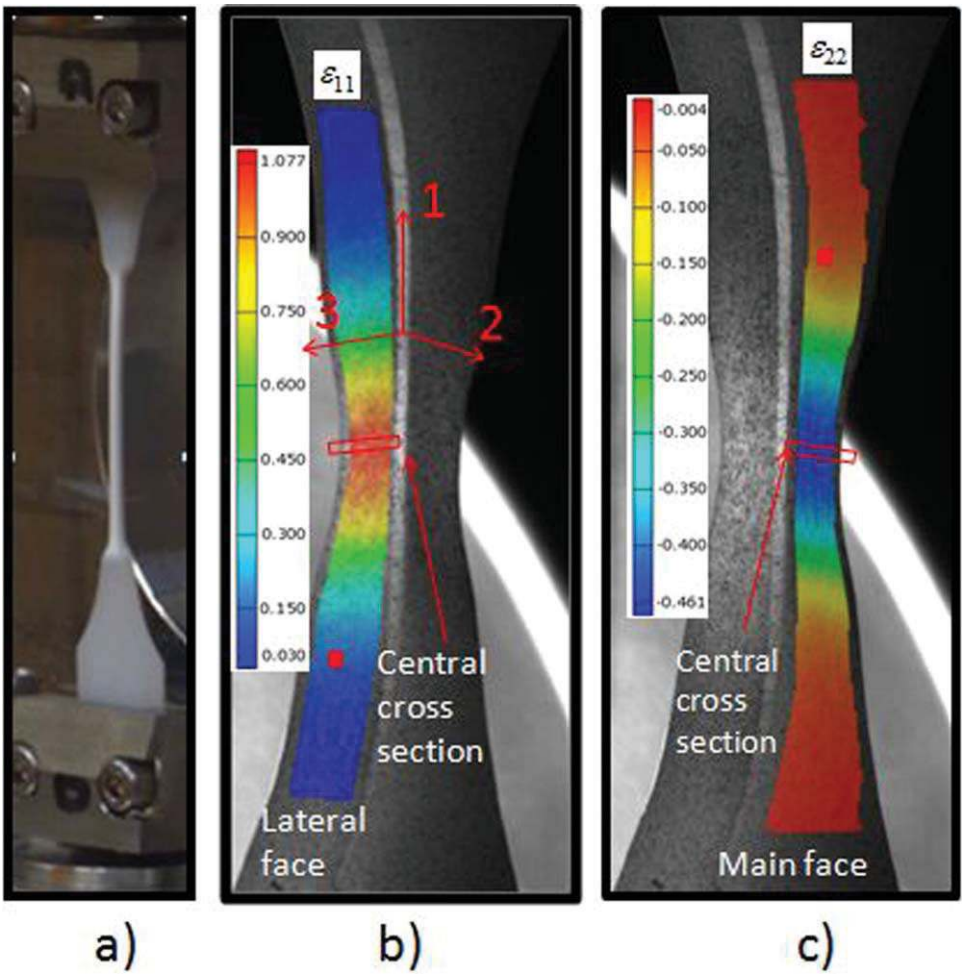

FIGURE 1 (a) Photograph of the specimen at the end of the test. Examples of ε_{11} strain map (b) and ε_{22} strain map (c). [Color figure can be viewed in the online issue, which is available at wileyonlinelibrary.com.]

strain ε_{11} (Axis 1: tensile axis) and the transverse strain ε_{22} (Axis 2 corresponds to the specimen width) were measured on the main specimen face, whereas a longitudinal strain map ε_{11} is also obtained for the lateral specimen face along with the other transverse strain map ε_{33} (Axis 3 corresponds to the specimen thickness). Figure 1 shows the specimen in the tensile machine at the end of the test [Fig. 1(a):$\varepsilon_{11} \approx 2$ in the specimen center] as well as the ε_{11} [Fig. 1(b)] and ε_{22} [Fig. 1(c)] strain maps, respectively, obtained on the lateral and main faces. The ε_{11} and ε_{33} strain maps were also simultaneously measured on the main and lateral faces. The results are not shown there but available in Ye et al.[24] [Fig. 7(c,d)]. In Figure 1, it can be seen that the strain values are much greater in the specimen central region where the neck has formed. By comparing the ε_{22} and the ε_{11} strain maps, it is possible to check that the Poisson's ratio value is close to 0.5. The ε_{33} strain map is very similar to that corresponding to ε_{22}, although we showed in a previous study[23] that it is not possible to use the assumption of a transversally isotropic deformation state to accurately evaluate the volume strain. The volume strain must be obtained with separate measurements for ε_{22} and ε_{33} and is given by: $\varepsilon_v \quad \varepsilon_{11}+\varepsilon_{22}+\varepsilon_{33}$

For the volume strain results used in this work, the ε_{11}, ε_{22}, and ε_{33} values were averaged on the specimen central cross-section.

DIC whole-field strain measurements were also carried out in the same conditions as those corresponding to the WAXS experiments, namely the same relative cross-head speed (20 μm s ^{1}), specimen shape, and tensile machine. This made it possible to obtain a calibration curve representing the cross-head displacement against the ε_{11} true strain in the central section. In the whole article, all the measured ε_{11} values were obtained in the central cross-section, which is also the center of the necking region. Figure 2 shows the $\Delta l(\varepsilon_{11})$ curve for the 100 WAXS measurement points.

WAXS EXPERIMENTS

Qualitative Analysis of the WAXS Patterns

The WAXS patterns recorded for strain levels corresponding to ε_{11} 0, ε_{11} 0.27, ε_{11} 0.58, ε_{11} 0.95, ε_{11} 1.5, and ε_{11} 1.8 are shown in Figure 3. At the undeformed state [Fig. 3(a)], the rings can be indexed using the orthorhombic unit cell for HDPE[21] (a_{ortho} 7.422Å, b_{ortho} 4.949Å, and c_{ortho} 2.544 Å).

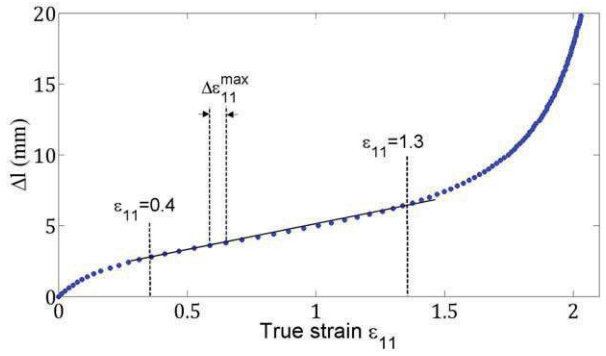

FIGURE 2 Calibration curve between the tensile machine cross head displacement Δl and the ε_{11} true strain in the central section. [Color figure can be viewed in the online issue, which is available at wileyonlinelibrary.com.]

The three first rings are: 110_{ortho}, 200_{ortho}, and 210_{ortho}. The diffuse intensity situated approximately in the vicinity of the 110_{ortho} reflection, and mainly in the ring inner part, corresponds to the amorphous halo [AH in Fig. 3(a)]. The martensitic transformation begins starting from $\varepsilon_{11} \approx 0.04$. The first three new reflections arising from the monoclinic phase are: $(001)_{\text{mono}}$, $(200)_{\text{mono}}$, and $(\bar{2}\,0\,1)_{\text{mono}}$ [see Fig. 3(b)]. The parameters of the monoclinic phase are: a_{mono} 8.085 Å, b_{mono} 2.544 Å, c_{mono} 4.808 Å, and β_{mono} 108.64°.[21] We should recall at this point that the chain direction corresponds to the *c*-axis for the orthorhombic form of HDPE and to the *b*-axis for the monoclinic form.

At high strain levels, the broadening of the crystallographic reflections [Fig. 3(e,f)] is a consequence of the average crystal sizes reduction caused by lamellae fragmentation. It is also evident by looking at the $I(2\theta)$ graphs that can be found in the Deconvolution Procedure subsection. In the subsection Apparent Crystal Size Evolution, we show a procedure, which enables us to estimate the broadening of crystallographic reflections and thus follow the lamellae fragmentation.

At the undeformed state [Fig. 3(a)], the intensity is approximately uniform along the diffraction rings, whereas a characteristic WAXS fiber pattern is obtained when the material is very deformed [Fig. 3(f)]. In the case of SCPs subjected to tensile deformation, fiber patterns are classically observed when the fibrillar morphology is established. The chains in the fragmented crystals and in the amorphous phase are then mainly oriented along the drawing axis. The normal vectors to the crystallographic planes parallel to the chain axis [$(h\,k\,0)$ for the orthorhombic phase and $(h\,0\,l)$ for the monoclinic one] are nearly situated along the equatorial plane. This plane also contains the incident X-ray beam and, therefore, the scattered intensity according to the laws of X-ray diffraction by crystals. In the WAXS pattern corresponding to Figure 3(f), some reflections whose intensity is not situated in the equatorial regions can also be observed in the upper right part of the figure. This corresponds to very enlarged and overlapping reflections from planes that are not parallel to the chains, more specifically the $(110)_{\text{mono}}$, $(011)_{\text{ortho}}$ $(1\,1\,\bar{1})_{\text{mono}}$, $(111)_{\text{ortho}}$, and $(201)_{\text{ortho}}$ reflections.

In the following, we will analyze particularly the $(1\,1\,0)_{\text{ortho}}$ and $(200)_{\text{ortho}}$ reflections for which X-ray intensity concentrates along the equatorial axis during the establishment of the fibrillar morphology. More precisely, intensity concentration along the equator arises from fragmented crystals while aligning their chains along the drawing axis. In Figure 4, we show the X-ray normalized intensity distribution along the rings ($I(\varphi)$), for several deformation states [Fig. 4(a): 110_{ortho} reflection and Fig. 4(b): $(200)_{\text{ortho}}$ reflection]. Angle φ is defined in Figure 3(a). The normalization is obtained by dividing the intensity by the curve area.

In the case of the intensity profile measured along the 200_{ortho} ring [$(I_{200}^{\text{ortho}}(\varphi))$: Fig. 4(b)], from the beginning of the deformation process and when the morphology is still lamellar, the intensity maximum (B) is situated along the equatorial axis $(\varphi \quad 0)$. Consequently, for the $(2\,0\,0)_{\text{ortho}}$ reflection, it is difficult to detect the specific signal corresponding to the establishment of the fibrillar morphology. The specific location of this maximum results here from the fact that {100} planes are easy slip planes. The detailed explanation can be found in Hiss et al.[5] (see particularly Fig. 23 of this reference and the corresponding comments).

For the intensity profile obtained along the $(110)_{\text{ortho}}$ ring ($I_{110}^{\text{ortho}}(\varphi)$), the maximum (L) was found to be situated at varying oblique orientations [see Figs. 3(b–e) and Fig. 4(a) for ε_{11} in the range 0.27–1.8]. In that case, the specific location of this maximum, neither along the equator nor along the meridian, shows that interlaminar and intralaminar slips proceed simultaneously.[5] The *L* maximum is observable from the beginning of the deformation process and can, therefore, be associated to the lamellar morphology.[5,25] On the $I_{110}^{\text{ortho}}(\varphi)$ profile, this maximum can clearly be distinguished up to ε_{11} 1.80, but it has completely disappeared for ε_{11} 1.99 [Fig. 4(a)]. Furthermore, in the strain range $(\varepsilon_{11} > 1.5)$ corresponding to the progressive disappearance of the *L* maximum, significant increase of the intensity at φ 0 occurs. For ε_{11} 1.73 and ε_{11} 1.79, it results in a secondary maximum (F) located at φ 0. The progressive appearance of this secondary maximum (F) is a consequence of the fibrillar morphology establishment. More specifically, for the $(110)_{\text{ortho}}$ reflection, the intensity increase at φ 0 mainly results from the increase in number of fragmented crystals, with chains aligned along the drawing axis. For our study, this made it possible to define an index quantifying the proportion of fragmented crystals which reoriented to align their chains along the drawing axis during the establishment of the fibrillar phase (see subsection Reorientation of the Fragmented Crystals and of the Amorphous Phase). However, careful study of Figure 3 shows that the amorphous halo (AH), mainly situated between the $(0\,0\,1)_{\text{mono}}$ and $(1\,1\,0)_{\text{ortho}}$ rings, also reoriented toward the equatorial direction. This is particularly clear when jumping from Figure 3(c) to 3(d) and finally to 3(e). This was also quantified with the analysis

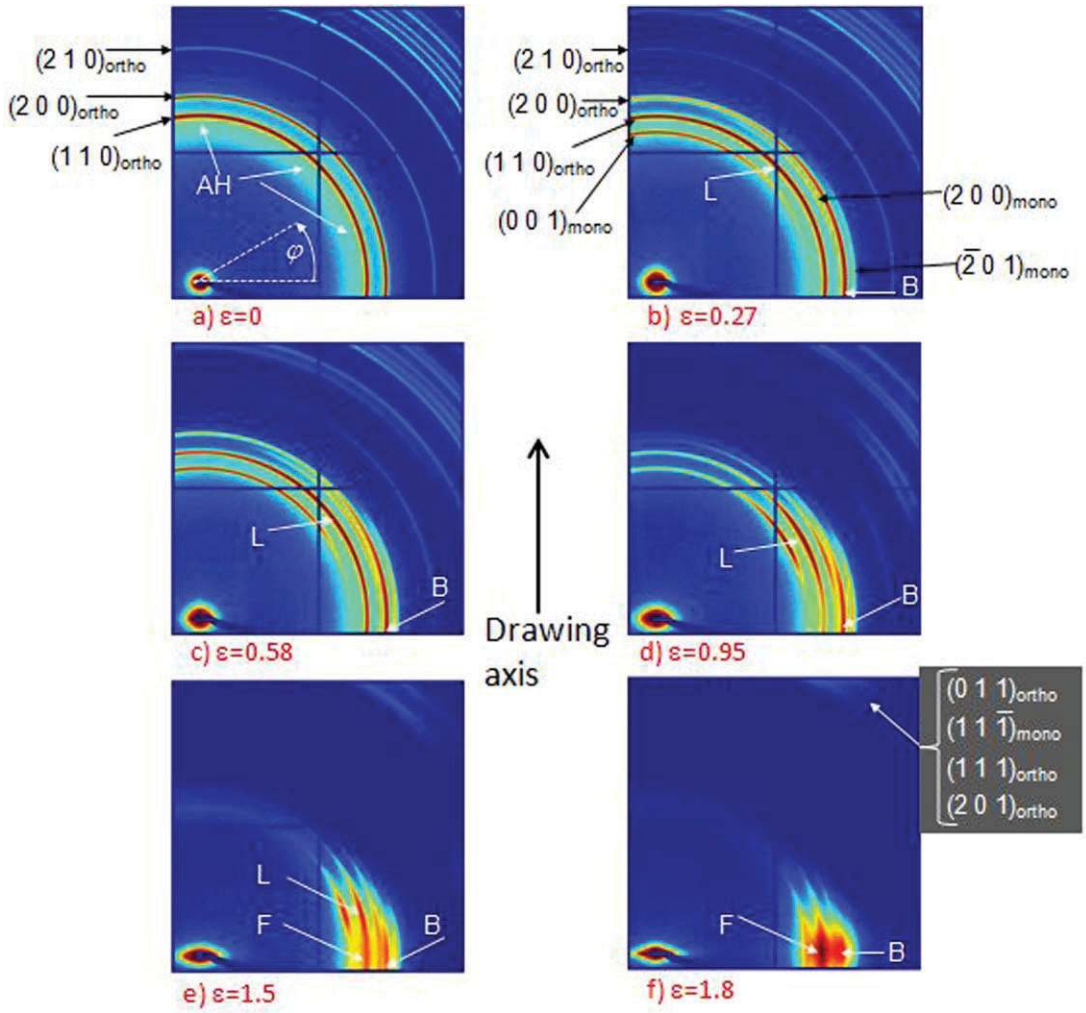

FIGURE 3 Dynamical sequence of WAXS patterns at six characteristic strains (logarithmic scale). [Color figure can be viewed in the online issue, which is available at wileyonlinelibrary.com.]

presented in subsection Reorientation of the Fragmented Crystals and of the Amorphous Phase. Finally, it should be noted that the intensity of the different peaks can overlap in the WAXS patterns shown in Figure 3, particularly the intensity of the 110_{ortho} reflection and the amorphous halo, even for the undeformed state. It is, therefore, necessary to

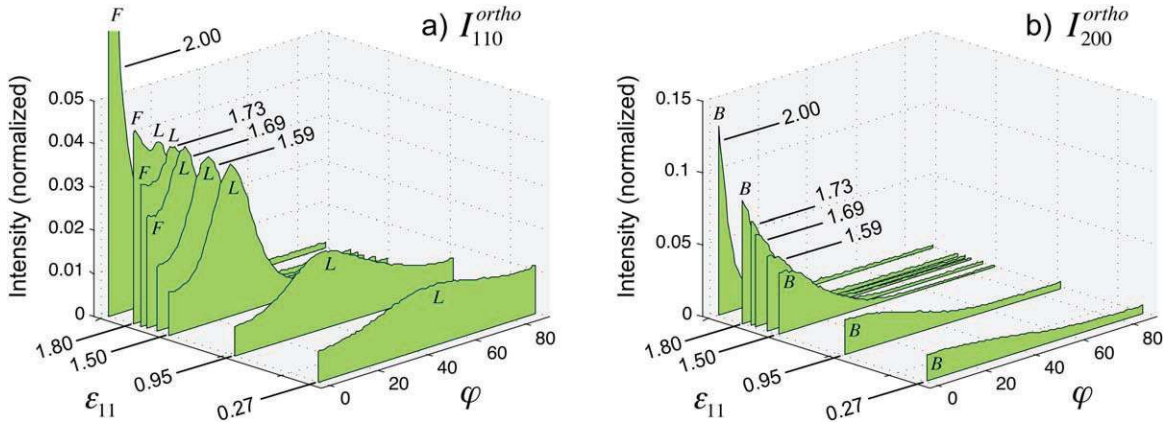

FIGURE 4 X ray normalized intensity along the diffraction rings for the $(1\,1\,0)_{ortho}$ and $(2\,0\,0)_{ortho}$ reflections. [Color figure can be viewed in the online issue, which is available at wileyonlinelibrary.com.]

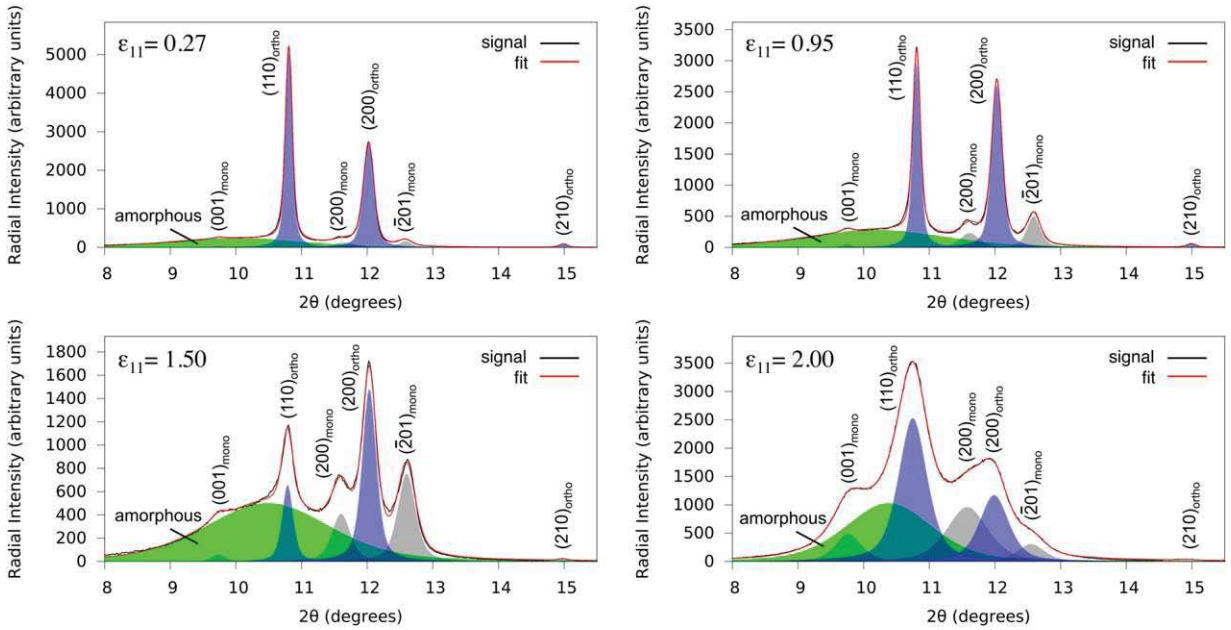

FIGURE 5 Examples of results obtained with the deconvolution procedure. [Color figure can be viewed in the online issue, which is available at wileyonlinelibrary.com.]

deconvolute the different peaks to carry out a relevant quantitative analysis. This is the aim of the following section.

Quantitative Analysis of the WAXS Patterns

Deconvolution Procedure

The objective of the deconvolution procedure is to extract the individual contributions of each peak from the total signal. The deconvolution procedure was carried out for intensity profiles $I(2\theta)$ taken along the φ 0°, and φ 45° directions and for $I(2\theta)$ profiles averaged along all the azimuthal angles: $\varphi \in [0°, 90°]$. Examples of $I(2\theta)$ profiles along the φ 0° direction are shown in Figure 5.

After subtraction of incoherent scattering, the $I(2\theta)$ profiles were approximated by the sum of several Pearson VII functions.[26] Each Pearson VII function was associated to a given peak. The Pearson VII function has the form:

$$f(2\theta) \quad \frac{A}{\left[1+4\left(\frac{2\theta \quad 2\theta_{hkl}}{\Delta(2\theta_{hkl})}\right)^2 (2^{1/m} \quad 1)\right]^m}$$

For the crystallographic reflections, θ_{hkl} is the Bragg angle. In this case, we, therefore, used a known parameter, but one which is fitted for the peak associated to the amorphous halo. For each peak A, m, and $\Delta(2\theta_{hkl})$ are fitted parameters which characterize the peaks shapes. A is the peak height; it is the only parameter directly obtained with the fit procedure that depends on the intensity of the incident beam. $\Delta(2\theta_{hkl})$ is the full width at half maximum. m is the shape parameter of the function, which can be interpreted as follows: when m 1, the Pearson VII distribution reduces to the Cauchy function and when $m \to \infty$, the Pearson VII takes the Gaussian form.

In the case of polyethylene, in the $2\theta \in [5° \; 16°]$ range of our study, a minimum of four bands or envelopes was expected in the undeformed state: the amorphous halo and three orthorhombic crystalline reflections with miller indices $(1\,1\,0)$, $(2\,0\,0)$, and $(2\,1\,0)$ (see subsection Qualitative Analysis of the WAXS Patterns). A maximum of seven bands was expected as soon as deformation proceeds with the three additional bands corresponding to monoclinic crystalline reflections with miller indices $(0\,0\,1)$, $(2\,0\,0)$, and $(\overline{2}\,0\,1)$. The other crystallographic reflections correspond to Bragg angles, which are significantly larger than 2θ 16° and not supposed to overlap in the $2\theta \in [5° \; 16°]$ interval. Peak profiles were deconvoluted using the PEAKFIT software.[27]

The number of peaks was adjusted depending on their visibility in the 1D signal. For example, we deliberately ignored very small monoclinic peaks rather than leaving the fitting procedure to detect these with a too significant error factor. Several trials on a given set of diffraction data were performed to find the optimum peak parameters corresponding to the minimum relative error between the fitted curve (red curve in Fig. 5) and the experimental curve (gray curve in Fig. 5). In Figure 5, we also show the individual contributions of each peak determined through our procedure. The colored-in curves show the amorphous halo (large bump) and the orthorhombic reflections (sharp peaks). At the end of the deconvolution procedure, the evolution of the parameters that characterize the peak shape (height, width, area, etc.) are known throughout the deformation process for different φ values. The physical meaning of these parameters can be analyzed using simple results from X-ray diffraction theory. It is then possible to construct some observables describing the microstructure evolution during the deformation process.

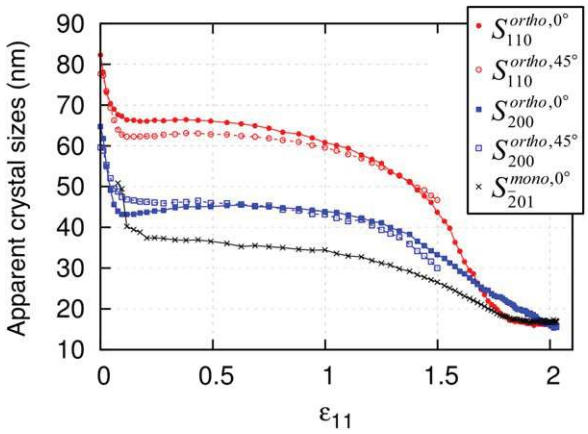

FIGURE 6 Apparent crystal sizes versus ε_{11}. [Color figure can be viewed in the online issue, which is available at wileyonlinelibrary.com.]

Apparent Crystal Size Evolution

By studying the changes of the diffraction peak widths, it is possible to obtain insight about the crystal size evolution during the test.

The coherent lengths associated to the different crystals dimensions are given by Scherrer's equation:

$$S_{hkl}(\varepsilon_{11}) \quad \frac{0.9\lambda}{\beta_{hkl}(\varepsilon_{11})\cos\theta_{hkl}}$$

Here, S_{hkl} is the coherent length associated with the $(h\,k\,l)$ reflection. λ is the X-ray radiation wavelength, θ_{hkl} is the Bragg angle, and β_{hkl} $\Delta(2\theta_{hkl})$ is the width of the diffraction peak. $\Delta(2\theta_{hkl})$ and, thereby, S_{hkl} change during the deformation process. To obtain $S_{hkl}(\varepsilon_{11})$, we need to estimate the width of the diffraction peaks $\Delta(2\theta_{hkl})$ during the deformation process, which was possible using the deconvolution procedure just described. The other quantities entered into Scherrer's equation are known parameters. Logically, the most accurate results are obtained for larger peaks: $(110)_{\text{ortho}}$, $(200)_{\text{ortho}}$, and $(\bar{2}\,0\,1)_{\text{mono}}$, and therefore, the results will be given for these three reflections in the following.

For a perfect crystal, the coherent length S_{hkl}, as defined by Scherrer's equation, is the average crystal size along the direction perpendicular to the $(h\,k\,l)$ planes. In the case of SCPs, the granular substructure of crystalline lamellae (see the Introduction section) causes loss of the "crystalline order," which results in significant broadening of the diffraction peaks. The S_{hkl} values are, therefore, expected to be smaller than the actual lamellae dimensions.[1,3] However, the S_{hkl} values also depend on changes to crystal sizes, which occur during the deformation process. In particular, crystal fragmentation causes the broadening of diffraction peaks and, therefore, a reduction of the coherent length S_{hkl}.[28,29] The evolution of the measured coherent lengths is, therefore, directly related to the reduction in crystal size. In the following, the coherent lengths S_{hkl} will be called "apparent sizes."

However, we are aware that the actual crystal sizes may be significantly larger particularly at the undeformed state. Readers also need to bear in mind the fact that schematically two distinct phenomena can lead to a decrease in the measured apparent crystal sizes:

1. Crystal fragmentation leading to a reduction of the actual crystal sizes.
2. Changes of the crystals (or lamellae) internal structure leading to a loss of "global crystalline order": blocky substructure at the lamellae scale. During the deformation process, the appearance of dislocations in the crystals can also greatly affect the crystal periodicity and contribute to peaks broadening.[30,31]

Figure 6 shows the evolution of the $S_{110}^{\text{ortho},0^\circ}$, $S_{110}^{\text{ortho},45^\circ}$, $S_{200}^{\text{ortho},0^\circ}$, $S_{200}^{\text{ortho},45^\circ}$, and $S_{201}^{\text{mono},45^\circ}$ apparent sizes. The WAXS intensity signal accumulation along the equatorial axis at high strain levels made it impossible to plot the apparent sizes measured along the 45° axis for strain larger than ε_{11} 1.5. From $\varepsilon_{11} \approx 0.08$, the proportion of formed monoclinic phase was sufficient for plotting $S_{201}^{\text{mono},45^\circ}$. All the curves shown in Figure 6 have more or less the same appearance. Before the yield point ($\varepsilon_{11} \approx 0.1$), the apparent sizes were found to decrease significantly, whereas after the yield point, a plateau region can be observed for these curves up to $\varepsilon_{11} \approx 0.5$. In the $\varepsilon_{11}[\in 0.5 \quad 1.7]$ strain range, the apparent sizes decreased significantly, whereas for $\varepsilon_{11} > 1.7$, they became approximately constant. These results are analyzed further in the Discussion section.

Reorientation of the Fragmented Crystals and of the Amorphous Phase

In this section, we shall present procedures enabling the quantification of the reorientation dynamics of the crystals and of the chains in the amorphous phase during the establishment of the fibrillar morphology. The objective was to determine the strain ranges during which each component reorients to become fully aligned along the drawing axis.

As previously mentioned, for the $(110)_{\text{ortho}}$ reflection, the intensity situated along the equatorial axis (0° axis) mainly arises from fragmented crystals, with chains reoriented along the drawing axis. A crystal reorientation index can, thus, be defined as follows: I^{CR} $A_{110,\text{ortho}}^{0^\circ}/A_{110,\text{ortho}}^{\text{total}}$. $A_{110,\text{ortho}}^{0^\circ}$ is the average area of the $(110)_{\text{ortho}}$ peak on the equatorial axis, calculated over the $\varphi \in [0^\circ\ 2^\circ]$ angular sector with φ azimuthal angle defined in Figure 3(a). $A_{110,\text{ortho}}^{\text{total}}$ is the average area of the same peak but calculated over the whole ring ($\varphi \in [0^\circ\ 90^\circ]$). Thanks to the deconvolution procedure, only the intensity corresponding to the $(1\,1\,0)_{\text{ortho}}$ reflection is taken into account. Because it is obtained by dividing by $A_{110,\text{ortho}}^{\text{total}}$, I^{CR} does not depend on the absolute X-ray intensity value. The I^{CR} variable increases if the crystals have reoriented to almost perfectly align their chains along the drawing axis during the fibrillar morphology's establishment phase. This index was essentially constructed to detect and analyze the intensity increase associated to the secondary

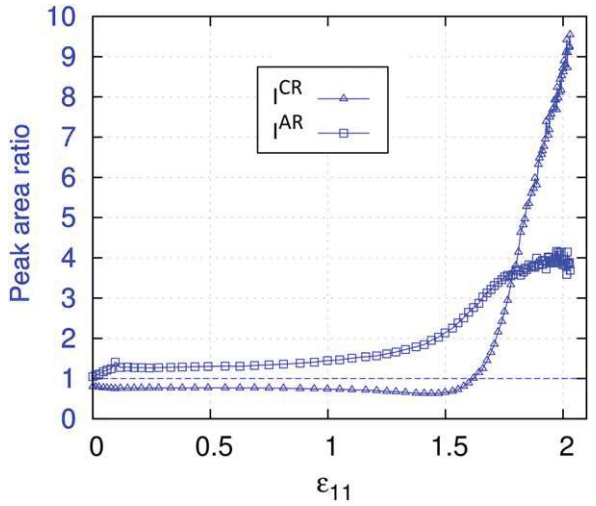

FIGURE 7 Reorientation indexes: I^{CR} (crystals) and I^{AR} amorphous chains versus ε_{11}. [Color figure can be viewed in the online issue, which is available at wileyonlinelibrary.com.]

maximum, which appears for the $(1\,1\,0)_{ortho}$ reflection (F in Fig. 4). It should be borne in mind that this secondary maximum is associated to the fibrillar morphology (see subsection Qualitative Analysis of the WAXS Patterns). Therefore, this index is significantly different from an average orientational order parameter like Hermann's factor, for instance, which quantifies the orientation degree of a family of lattice planes.[32] The $I^{CR}(\varepsilon_{11})$ plot is shown in Figure 7. The I^{CR} variable remained approximately constant up to $\varepsilon_{11} \approx 1.5$ and then increased very strongly.

Similar processing work can be carried out for the amorphous halo. Monar and Habenschuss[33] have shown that for polyethylenes, the amorphous halo in WAXS patterns arises mainly from intermolecular scattering. The intensity of the amorphous halo situated along the equatorial axis is, thus, due to scattering from polymer chains aligned along the drawing axis.[34] The amorphous phase reorientation index can, therefore, be defined as follows: I^{AR} $A^{0^\circ}_{amorphous}/A^{total}_{amorphous}$, with

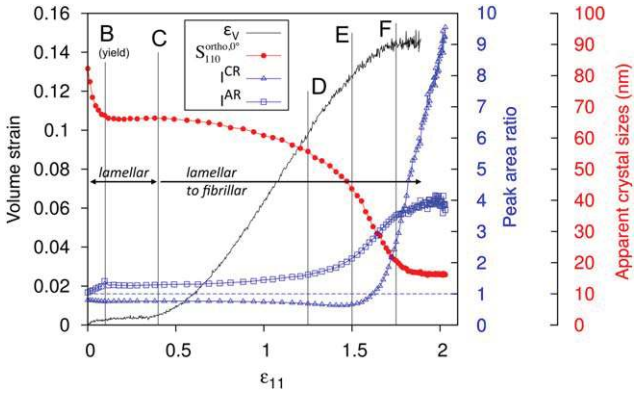

FIGURE 8 Volume strain ε_v, $S^{ortho,0^\circ}_{110}$ apparent crystal size, and reorientation indexes I^{CR} (crystals) and I^{AR} (amorphous chains) versus ε_{11}. [Color figure can be viewed in the online issue, which is available at wileyonlinelibrary.com.]

$A^{0^\circ}_{amorphous}$ and $A^{total}_{amorphous}$ defined in the same way as for the $(1\,1\,0)_{ortho}$ crystal peaks. The I^{AR} variable increases when there are an increasing proportion of polymer chains in the amorphous phase, with local direction oriented along the stretching axis. The evolution of the I^{AR} variable is shown in Figure 7. Before the yield point (ε_{11} 0.1), a significant increase in I^{AR} was observed. Next, in the $\varepsilon_{11} \in [0.1 \quad 1.3]$ strain range, I^{AR} was found to increase slightly, whereas from $\varepsilon_{11} \approx 1.3$, I^{AR} increased strongly.

In the Discussion section, for analyzing the microstructural transformations occurring during the deformation process, the variables $S^{ortho,0^\circ}_{110}(\varepsilon_{11})$, $I^{CR}(\varepsilon_{11})$, and $I^{AR}(\varepsilon_{11})$ are put in relation with the volume strain evolution.

DISCUSSION

Between 1999 and 2005, significant progress was achieved in understanding SCPs' deformation mechanisms through the works of Strobl and coworkers.[5–9,32] A very general pattern was highlighted corresponding to different stages with specific deformation mechanisms during the deformation process. The transitions between these regimes occur at critical strain values that are denoted by points A, B, C, and D in the articles of the Strobl's research group:

- Point A, $\varepsilon_{11} \approx 0.03$: onset of slips of individual crystalline blocks inside the lamellae. Point A corresponds to the onset of the plastic deformation process in lamellae and, therefore, to the end of the pure viscoelastic regime. However, before the yield point ($\varepsilon_{11} \approx 0.1$), deformation still occurs mainly in the amorphous phase.
- Point B ≈ yield point, $\varepsilon_{11} \approx 0.1$: change into a collective activity of slips of the crystalline blocks inside the lamellae leading to strong lamellae plastic deformation
- Point C ($\varepsilon_{11} \approx 0.4$ 0.6 about 0.4 for HDPE): onset of lamellae fragmentation
- Point D ($\varepsilon_{11} \approx 1.1$): onset of chain disentanglement.

It should be noted that each block still belongs to a certain lamella up to Point C and that the lamellar structure is then globally preserved.

To analyze the link between phenomena occurring at the crystal level and polymer macroscopic dilatation, we show in a same figure the evolution of $I^{AR}(\varepsilon_{11})$, $I^{CR}(\varepsilon_{11})$, $S^{ortho,0^\circ}_{110}(\varepsilon_{11})$, and $\varepsilon_v(\varepsilon_{11})$ (Fig. 8). The volume strain ($\varepsilon_v(\varepsilon_{11})$) evolution can be divided into three distinct regimes:

- in strain range $\varepsilon_{11} \in [0 \quad 0.4]$, the volume strain increase is very low,
- in strain range $\varepsilon_{11} \in [0.4. \quad 1.7]$, nearly all the volume strain increase takes place,
- at the end of the test, in strain range $\varepsilon_{11} \in [1.7 \quad 1.9]$, the volume strain remains nearly constant.

In the following, we shall show that at low strain levels, our work provides new insight into the general pattern developed by the Strobl's group. At higher strain levels, we show that it is possible to define other characteristic points during the deformation process.

Before the Yield Point ($\varepsilon_{11} \approx 0.1$: Point B)

Figures 7 and 8 show that, in the strain range $\varepsilon_{11} \in [0 \quad 0.1]$, the increase in the I^{AR} variable is much more pronounced than in the following $\varepsilon_{11} \in [0.1 \quad 0.4]$ interval. The I^{AR} index was constructed to describe the chains reorientation dynamics in the amorphous phase. As mentioned in the Introduction section, deformation is mainly concentrated in the amorphous regions of the polymer before the yield point.[4,15] Accordingly, it can be assumed that the strong increase in the I^{AR} index in strain range $\varepsilon_{11} \in [0 \quad 0.1]$ is the signature of the significant transformations, which occur in the amorphous regions before the yield point.

In addition, before the yield point (Point B), a significant reduction in the crystals apparent sizes can be observed (Fig. 6). It is difficult to find a simple interpretation for this experimental data because massive lamellae fragmentation would certainly not have begun at such small strain levels. Thus, the decrease in the measured apparent sizes cannot simply be associated with a reduction in the actual crystal sizes because of net and definitive lamellae breakages. The alternative option mentioned in the subsection Apparent Crystal Size Evolution needs to be examined, namely changes to the lamellae (or crystals) internal structure causing loss of the lamellae "global crystalline order" and thereby reducing the lamellae coherent lengths. In the case of an α isostatic polypropylene, a curve comparable with those shown in Figure 6 was already published (see Fig. 5 in Polt et al.[31] but for a smaller strain range ($\varepsilon_{11} \in [0 \quad 0.4]$). The trend is the same: As for the curves shown in Figure 6, before $\varepsilon_{11} \approx 0.1$ or $\varepsilon_{11} \approx 0.2$, the apparent size drops abruptly. In the following interval, $\varepsilon_{11} \in [0.2 \quad 0.4]$, the apparent size becomes approximately constant. In this article, the decrease in the apparent sizes is attributed to the increase in the dislocation density. Another interpretation is possible that provides an explanation regarding the key role played by the yield point (Point B in Fig. 8). At the undeformed state, the existence of crystal blocks inside the lamellae (lamella substructure) causes reduction in the measured apparent sizes (see subsection Apparent Crystal Size Evolution). Strobl and coworkers have shown that the individual slips of crystal blocks in lamellae start and then develop for strain levels (Point A, $\varepsilon_{11} \approx 0.03$) significantly smaller than the level corresponding to the yield point. We can, therefore, assume that the slips of individual crystal blocks cause relative displacement of the adjacent blocks, resulting in a loss of overall crystalline order and thereby a decrease in the coherent lengths. Accordingly, up to Point A (roughly the second measurement point), the apparent sizes should remain constant. This can be seen on the $S_{200}^{\text{ortho},45^\circ}$ and $S_{110}^{\text{ortho},45^\circ}$ curves (Fig. 6). For the $S_{200}^{\text{ortho},0^\circ}$ and the $S_{110}^{\text{ortho},0^\circ}$ curves, the curve drop was simply found to be smaller in the $\varepsilon_{11} \in [0 \quad 0.03]$ interval than in the following $\varepsilon_{11} \in [0.03 \quad 0.08]$ interval.

For the purposes of further analysis, it would be interesting to carry out new experiments with many more measurement points for very low strain levels. However, the drop of the crystals' apparent sizes observed before the yield point proves that the crystals undergo significant transformations in this strain range.

Between the Yield Point ($\varepsilon_{11} \approx 0.1$: Point B) and Point C ($\varepsilon_{11} \approx 0.4$)

Clearly, from Point B ($\varepsilon_{11} \approx 0.1$) to Point C ($\varepsilon_{11} \approx 0.4$), the crystal apparent sizes were found to remain approximately constant (see Figs. 6 and 8), which shows that crystal fragmentation was yet to occur in this strain range. The morphology is, therefore, still lamellar, which complies with the results obtained by Strobl and coworkers.[5–9,32] In the strain range $\varepsilon_{11} \in [0 \; 0.4]$, the lamellar structure can still be deformed "continuously" without losing its overall integrity. It should be noted that, at the lamellae level, Point B is characterized by a change from individual block slips to collective block slips.[5] The fact that the crystal sizes remain constant shows that, unlike individual block slips, collective slips of crystalline blocks do not significantly affect the "global crystalline order." In the strain range $\varepsilon_{11} \in [0.1 \quad 0.4]$, the increase in the volume strain ε_v was found to be very low (see Fig. 8). The lamellar structure that still exists strongly limits the cavitation phenomenon. Only nanovoids embedded between lamellae can develop in the polymer, and these nanovoids were detected using small-angle X-ray scattering measurements.[22]

Strain Range ε_{11}>0.4 (from Lamellar to Fibrillar)

From a strain between $\varepsilon_{11} \quad 0.35$ and $\varepsilon_{11} \quad 0.6$, the onset of a decrease phase can be detected (see the $S_{110}^{\text{ortho},0^\circ}$ and $S_{110}^{\text{ortho},45^\circ}$ curves) for the apparent sizes measured perpendicularly to the $(1\,1\,0)_{\text{ortho}}$ planes. Overall, this decrease phase extends in strain range $\varepsilon_{11} \in [0.4 \quad 1.7]$. This reduction in the crystal apparent sizes was certainly a consequence of progressive lamellae fragmentation. This fits well with the aforementioned Strobl pattern because the decreasing phase starts approximately for a strain level corresponding approximately to Point B. For the dimension perpendicular to the $(2\,0\,0)_{\text{ortho}}$ planes, the $S_{200}^{\text{ortho},0^\circ}$ and $S_{200}^{\text{ortho},45^\circ}$ decrease was detectable later, for about $\varepsilon_{11} \approx 0.7$ (Fig. 6). This difference can be explained by the fact that the lamellae may break first along their smallest section; in other words, along the $(0\,1\,0)_{ortho}$ planes. Fractures along these planes lead to the reduction of S_{110}^{ortho} but not of S_{200}^{ortho}. In contrast, lamellae fractures along the $(1\,0\,0)_{\text{ortho}}$ planes cause both S_{110}^{ortho} and S_{200}^{ortho} to diminish. The size evolution of the monoclinic phase was analyzed by plotting $S_{-201}^{\text{mono},0^\circ}(\varepsilon_{11})$. Starting from $\varepsilon_{11} \quad 0.08$, the quantity of the formed monoclinic phase was sufficient to enable the measurement of apparent crystallite size. Overall, the curve displays the same features as those corresponding to the orthorhombic phase. In Figure 8 where the plots corresponding to $S_{110}^{\text{ortho},0^\circ}$ and ε_v are superposed, the onset of crystal fragmentation can clearly be seen to occur at the same strain level ($\varepsilon_{11} \approx 0.4$) as the beginning of the phase of strong volume strain increase. Moreover, the lamellae fragmentations, evidence of which is the decrease in the crystal apparent sizes, mainly occur in strain range $\varepsilon_{11} \in [0.4 \; 1.7]$. This corresponds exactly to the strain range where the volume strain increased significantly. For strain

levels larger than ε_{11} 1.7, the apparent crystal sizes were found to progressively reach a constant value. In the same strain range, the volume strain also becomes constant. In conclusion, we have highlighted a strong correlation between the evolution of apparent crystal sizes and the volume strain curve. This proves that for the SCP under study, the cavitation phenomenon occurs mainly during the crystal fragmentation phase. As previously mentioned, before Point C, the existing lamellar skeleton only permits the formation of nanovoids between the lamellae.

This link between lamellae fragmentation and cavitation has already been mentioned in previous studies. Addiego et al.[16] suggested that the fragmentation of lamellae causes the development of heterogeneities, voids, or very low density regions situated in the vicinity of the fracture regions. As Galeski[4] and Pawlak et al.[15] noted, the Peterlin representation[18] widely used to simply describe the lamellar morphology destruction inherently implies cavitation. For a clear illustration of this phenomenon, readers may refer to Figure 13 of the Galeski article[4] and the comments on that figure.

The I^{AR} variable (Figs. 7 and 8) increases during the whole deformation process, but from $\varepsilon_{11} \approx 1.2$ or $\varepsilon_{11} \approx 1.3$, this increase becomes much more pronounced, which shows that the amorphous chains significantly reorient toward the drawing axis. Interestingly, this strain value is very close to that identified as the onset of chain disentanglement (Point D, $\varepsilon_{11} \approx 1.1$) in the works of Strobl and coworkers.

For $\varepsilon_{11} \approx 1.5$ (Point E), the I^{CR} variable was found to start increasing. For $\varepsilon_{11} \approx 1.7$, the I^{CR} slope becomes maximum. It is interesting to note that the reorientation of crystals occurred very suddenly; before $\varepsilon_{11} \approx 1.5$, I^{CR} was nearly constant; then, for $\varepsilon_{11} > 1.5$, the I^{CR} increase became very abrupt. The amorphous halo began to accumulate in the equatorial region for strains smaller than $\varepsilon_{11} \approx 1.5$ (see the I^{AR} curve in Fig. 8), and the amorphous halo overlaps with the $(110)_{ortho}$ reflection (Fig. 5). So the sudden alignment of crystals, which occurred for $\varepsilon_{11} \approx 1.5$ in relation with the establishment of the fibrillar morphology, would be very difficult to highlight by using the raw WAXS patterns. This is a good illustration of the necessity for a preliminary peaks deconvolution procedure before analyzing the WAXS data. It can be assumed that between $\varepsilon_{11} \approx 1.5$ and $\varepsilon_{11} \approx 1.7$, the initial lamellar skeleton becomes completely disarticulated. Consequently, the fragmented crystals have new degrees of freedom and can reorient to align their chains along the drawing axis (see Figs. 7 and 8 for $\varepsilon_{11} > 1.7$). At the same time, for ε_{11} larger than 1.7 (Point F in Fig. 8), the crystals nearly reached their final sizes, and the volume strain was constant (see Fig. 8 for $\varepsilon_{11} > 1.7$). This suggests that when the fragmented crystals become free to rotate to align their chains along the drawing axis, crystal fragmentation is no longer required to allow material deformation. Deformation mainly results from chain stretching in the amorphous phase, leading to a strong strain hardening as can be observed at the end of the true stress/true strain curve [see, for example, the tensile curves shown in Fig. 9(a) in Farge et al.[23] for the same material].

CONCLUSIONS

In this study of a HDPE deformed in tension, we have highlighted a clear correlation between the volume strain increase and the decrease in apparent lamellae sizes. This shows that the cavitation phenomenon is linked with the progressive fragmentation of lamellae, which occurs during the lamellar/fibrillar transition. At the end of the deformation process, when the lamellar morphology is destroyed, the fragmented crystals have new degrees of freedom and can freely rotate to align their chains along the drawing axis. Crystal fragmentation is then no longer needed to allow material deformation, and there is no further volume strain increase.

REFERENCES AND NOTES

1 T. Hippler, S. Jiang, G. Strobl, *Macromolecules* **2005**, *38*, 9396 9397.

2 G. Strobl, *Prog. Polym. Sci.* **2006**, *31*, 398 442.

3 S. Patlazhan, Y. Remond, *J. Mater. Sci.* **2012**, *47*, 6749 6767.

4 A. Galeski, *Prog. Polym. Sci.* **2003**, *28*, 1643 1699.

5 R. Hiss, S. Hobeika, C. Lynn, G. Strobl, *Macromolecules* **1999**, *32*, 4390 4403.

6 S. Hobeika, Y. Men, G. Strobl, *Macromolecules* **2000**, *33*, 1827 1833.

7 Y. Men, G. Strobl, *J. Macromol. Sci. Phys.* **2001**, *40*, 775 796.

8 Y. Men, G. Strobl, *Macromolecules* **2003**, *36*, 1889 1898.

9 Q. Fu, Y. Men, G. Strobl, *Polymer* **2003**, *44*, 1927 1933.

10 K. Hong, A. Rastogi, G. Strobl, *Macromolecules* **2004**, *37*, 10165 10173.

11 M. F. Butler, A. M. Donald, W. Brass, G. R. Mant, G. E Derbyshire, A. J. Ryan, *Macromolecules* **1995**, *28*, 6383 6393.

12 M. F. Butler, A. M. Donald, A. J Ryan, *Polymer* **1998**, *39*, 39 52.

13 K. Schneider, S. Trabelsi, N. E. Zafeiropoulos, R. Davies, C. Riekel, M. Stamm, *Macromol. Symp.* **1999**, *236*, 441 448.

14 A. Pawlak, *Polymer* **2007**, *48*, 1397 1409.

15 A. Pawlak, A. Galeski, A. Rozanski, *Prog. Polym. Sci.* **2014**, *39*, 921 958.

16 F. Addiego, A. Dahoun, C. G'sell, J. M. Hiver, O. Godard, *Polym. Eng. Sci.* **2009**, *49*, 1198 1205.

17 L. Ruihua, X. Wenfei, N. Bing, Q. Zhang, Q. Fu. *J. Polym. Sci. Part B: Polym. Phys.* **2008**, *46*, 1202 1206.

18 A. Peterlin, In Polymeric Materials; E. Baer, Ed.; American Society for Metals: Metals Park, OH, **1975**; pp 175 195.

19 T. Seto, T. Hara, K. Tanaka, *Jpn. J. Appl. Phys.* **1968**, *7*, 31 42.

20 M. Bevis, B. Crellin, *Polymer* **1971**, *12*, 666 684.

21 K. E Russel, B. K. Hunter, R. D. Heynding, *Polymer* **1997**, *38*, 1409 1414.

22 R. Eriksen, C. Berggreen, S. W. Boyd, J. M. Dulieu Barton, *EPJ Web of Conferences* **2010**, *6*, 31013.

23 L. Farge, S. André, F. Meneau, J. Dillet, C. Cunat, *Macromo lecules* **2013**, *46*, 9659 9668.

24 J. Ye, S. Andre, L. Farge, *Int. J. Solids Struct.*, in press.

25 M. E. Vickers, H. Fisher, *Polymer* **1995**, *36*, 2667 2670.

26 P. Sajkiewicz, T. Hashimoto, K. Saijo, A. Gradys, *Polymer* **2005**, *46*, 513 521.

27 T. C. O'Haver. Version 5.4; A pragmatic Introduction to sig nal Processing**1995**. Available at: http://terpconnect.umd.edu/~toh/spectrum/InteractivePeakFitter.htm, accessed on June 2014.

28 R. Bao, Z. Ding, G. Zhong, W. Yang, B. Xie, M. Yang, *Colloid Polym. Sci.* **2012**, *290*, 261 274.

29 R. Bao, Z. Ding, Z. Liu, W. Yang, B. Xie, M. Yang, *Polymer* **2013**, *54*, 1259 1268.

30 F. Spieckermann, G. Polt, H. Wilhelm, M. Kerber, E. Schafler, M. J. Zehetbauer, *J. Appl. Polym. Sci.* **2012**, *125*, 4150 4154.

31 G. Polt, F. Spieckermann, H. Wilhelm, M. B. Kerber, E. Schafler, S. Bernstorff, M. Zehetbauer, *Mech. Mater.* **2013**, *67*, 126 132.

32 K. Hong, G. Strobl, *Macromolecules* **2006**, *39*, 268 273.

33 K. Monar, A. Habenschuss, *J. Polym. Sci. Part B: Polym. Phys.* **1999**, *37*, 3401.

34 Z. Jiang, Y. Tang, J. Rieger, H. F. Enderle, D. Lilge, S. V. Roth, R. Gehrke, Z. Wu, Z. Li, Y. Men, *Polymer*, **2009**, *50*, 4101 4111.